Dimeric assembly of F_1-like ATPase for the gliding motility of *Mycoplasma*

Takuma Toyonaga[1,2], Takayuki Kato[3], Akihiro Kawamoto[3], Tomoko Miyata[4,5], Keisuke Kawakami[6], Junso Fujita[4,5,7], Tasuku Hamaguchi[8], Keiichi Namba[4,5], Makoto Miyata[1,2]

[1]Graduate School of Science, Osaka Metropolitan University, 3-3-138 Sugimoto, Sumiyoshi-ku, Osaka 558-8585, Japan

[2]The OMU Advanced Research Institute for Natural Science and Technology (OCARINA), Osaka Metropolitan University, 3-3-138 Sugimoto, Sumiyoshi-ku, Osaka 558-8585, Japan

[3]Institute for Protein Research, Osaka University, 3-2 Yamadaoka, Suita, Osaka 565-0871, Japan

[4]Graduate School of Frontier Biosciences, Osaka University, 1-3 Yamadaoka, Suita, Osaka 565-0871, Japan

[5]JEOL YOKOGUSHI Research Alliance Laboratories, Osaka University, 1-3 Yamadaoka, Suita, Osaka 565-0871, Japan

[6]Biostructual Mechanism Laboratory, RIKEN, SPring-8 Center, 1-1-1, Kouto, Sayo, Hyogo 679-5148, Japan

[7]Graduate School of Pharmaceutical Sciences, Osaka University, 1-6 Yamadaoka, Suita, Osaka 565-0871, Japan

[8]Institute of Multidisciplinary Research for Advanced Materials, Tohoku University,

2-1-1 Katahira, Aoba-ku, Sendai 980-8577, Japan

Corresponding author: Makoto Miyata; Email: miyata@omu.ac.jp

Present address: Takuma Toyonaga: Institute of Multidisciplinary Research for Advanced Materials, Tohoku University, 2-1-1 Katahira, Aoba-ku, Sendai 980-8577, Japan

Abstract

Rotary ATPases, including F_1F_o- and V/A-ATPases, are molecular motors that exhibit rotational movements for energy conversion[1]. In the gliding bacterium, *Mycoplasma mobile*, a dimeric F_1-like ATPase forms a chain structure with the glycolytic enzyme, phosphoglycerate kinase (PGK), within the cell[2], which is proposed to drive the bacterial gliding motility[2–4]. However, the mechanisms of force generation and transmission remain unclear. Here, we present a 3.2 Å resolution structure of the dimeric ATPase complex obtained using electron cryomicroscopy (cryo-EM). Notably, the structure revealed an assembly distinct from that of known dimeric forms of F_1F_o-ATPase[5], despite containing conserved F_1-ATPase structures. The two ATPase units were interconnected by GliD dimers, previously identified as MMOB1620[2,6]. Gliβ, a homologue of the F_1-ATPase catalytic subunit[6], exhibited a specific N-terminal region that incorporates PGK into the complex. Structural conformations of the catalytic subunits, catalytically important residues, and nucleotide-binding pattern of the catalytic sites of the ATPase displayed strong similarities to F_1-ATPase, suggesting a rotation based on the rotary catalytic mechanism conserved in rotary ATPases[1,7–10]. Overall, the

cryo-EM structure underscores an evolutionary connection in the rotary ATPases and provides insights into the mechanism through which F_1-like ATPase drives bacterial gliding motility.

Introduction

Rotary ATPases are molecular motors that link ATP hydrolysis or synthesis with ion transport via rotational motion in biological membranes[1]. These motors comprise two common domains: soluble R_1, which is responsible for ATP hydrolysis and synthesis, and membrane-embedded R_o, which is responsible for ion transport. F_1F_o-ATPase, one of the rotary ATPases conserved across most eukaryotes, archaea, and bacteria, is responsible for ATP synthesis and the maintenance of membrane potential[5]. An F_1-like ATPase gene cluster, referred to as Type 2 ATPase, was reported in four *Mycoplasma* species, *M. mobile*, *M. pulmonis*, *M. agassizii*, and *M. testudineum*, in addition to the genuine F_1F_o-ATPase gene cluster, referred to as Type 1 ATPase[11,12] (Extended Data Fig. 1). The presence of F_1-ATPase α and β subunit homologues (MMOBs 1660 and 1670 in *M. mobile*) in the Type 2 ATPase gene cluster suggests a shared evolutionary origin in the F_1 domain. Type 2 ATPase is proposed to drive the gliding motility observed in *M. mobile* and *M. pulmonis*[2–4,13,14]. *M. mobile*, a fish pathogen, glides at speeds of up to 4 µm per second on a solid surface covered with sialylated oligosaccharides found on host cell surfaces[15] (Fig. 1a, Extended Data Fig. 2). In our proposed model for gliding, filamentous leg structures on the mycoplasma cell surface, which are approximately 50 nm, propel the cell body by catching and pulling sialylated oligosaccharides on the solid surface. Inside the cell, motors composed of Type 2 ATPase and phosphoglycerate kinase (PGK), which converts ADP to ATP through glycolysis, are linked near the cell

membrane to form 'internal chains'[2,6]. The motor is formed by dimerised F_1-like ATPase units with unique bridge structures and is referred to as a twin motor. However, the mechanisms of force generation and transmission remain unclear. This study aimed to elucidate the detailed structure of the twin motor using cryo-EM single-particle analysis (SPA). Notably, the structural features had a strong homology to those of F_1-ATPase[7,8], suggesting a rotary catalytic mechanism analogous to that of rotary ATPase[1,9,10] for the gliding motility of *M. mobile*.

Results

Protein identification using the cryo-EM structure of twin motor

Cryo-EM SPA was performed for twin motors isolated from *M. mobile* cells using images collected on the epoxidised graphene grid (EG-grid)[16] (Extended Data Table 1). The overall 3D structure of the twin motor was determined at a resolution of 3.2 Å (Fig. 1b, Extended Data Figs. 3, 4). Local refinement improved the resolution of the regions, each containing the F_1-like ATPase unit, to 3.1 Å (Extended Data Figs. 3b, 4). The density maps enabled the construction of the atomic model of the twin motor (Fig. 1c). The modelled sequence regions of each subunit are summarised in Extended Data Table 2. The twin motor exhibited a rectangular structure with dimensions of approximately 350 × 250 × 150 Å and at least 24 polypeptide chains with a total mass of approximately 1.5 MDa. Notably, the two F_1-like ATPase units were inclined to each other by approximately 5° and formed a dimer with pseudo-two-fold rotational symmetry and several accessories (Fig. 1c, d). The F_1-like ATPase comprised a hexameric ring of two alternating subunits and a central shaft subunit, identified as MMOBs 1660, 1670, and 1630, respectively. In the present study, these subunits were

named Gliα, Gliβ, and Gliγ, according to the subunit names of F_1-ATPase[10]. In the hexameric ring, nucleotide-derived densities were observed at five of the six subunit interfaces, despite the isolation and analysis of samples under nucleotide free condition, indicating the presence of endogenous nucleotides as reported in F_1-ATPase[17] (Fig. 1c, e). The subunit attached to Gliα, forming a 'bridge' between two F_1-like ATPase units, was identified as MMOB1620 and named GliD in the present study (Fig. 1c). The three densities protruding from the dimeric F_1-like ATPase were identified as MMOB4530, which was previously annotated as PGK. The denoised 3D map revealed additional distinct densities at six locations, including the $PGK_{1–3}$ regions (Extended Data Fig. 5a). These six densities exhibited correlation coefficients ranging from 0.37 to 0.48 with the crystal structure of PGK from *Staphylococcus aureus* (PDB ID: 4DG5) (Extended Data Fig. 5b, c). Although the values are low, these assignments are consistent with the stoichiometry previously estimated via SDS-PAGE[2], suggesting these maps are PGK molecules. A density bound only to one of the two F_1-like ATPase units was identified as MMOB3660, which was newly detected via SDS-PAGE of the twin motor and named GliE in the present study (Fig. 1b, c, Extended Data Fig. 6). This small protein (112 aa), characterised by a β-sandwich, was nestled between the ATPase hexamer and other subunits, breaking the rotational symmetry of the complex (Extended Data Fig. 7). Although MMOB1640, encoded in the Type 2 ATPase gene cluster, was detected via SDS-PAGE of the twin motor (Extended Data Fig. 6), the protein density was not observed from the overall 3D map.

Structural features of subunits comprising F_1-like ATPase

Gliβ and Gliα exhibited high structural similarity to the β and α subunits of the

F_1-ATPase from the thermophilic bacterium, *Bacillus* PS3[8] (PDB ID: 8HH5), based on the superimposition of their Cα atoms with the root mean squared deviation (RMSD) values of 1.95 Å and 2.79 Å, respectively (Fig. 1g, i). Both Gliβ and Gliα had three domains: crown, nucleotide-binding domain (NBD), and C-terminal domain (CTD). The NBDs of Gliβ and Gliα comprise a phosphate-binding motif of P-loop[18], consisting of the amino acid sequences GGAGVGKT and GDRGTGKT, respectively (Fig. 1f, h). The Gliβ-CTD contained a DELSEED loop, which is important for torque transmission in the F_1-ATPase β subunit[19], with an amino acid sequence of DALSEDD (Fig. 1f). A remarkable difference between Gliβ and the F_1-ATPase β subunit was the presence of an extended N-terminal region consisting of the N-terminal domain (NTD) and linker (Fig. 1f, Extended Data Fig. 8a). This region comprised approximately 100 residues located within the extra N-terminal 299 residues of Gliβ[6,12]. Notably, the linker hangs outside the F_1-like ATPase along the crown and NBD (Extended Data Fig. 8b). Gliβ-NTDs, consisting of 4 to 6 helices, were oriented in various directions among Gliβ, depending on their position in the complex (Extended Data Fig. 8a, c, d). Further, Gliβ-NTD interacted with PGK (Fig. 2a, b). In addition, at the interface of the two F_1-like ATPase units, the N-terminal regions of $Gli\beta_3$ and $Gli\beta_6$ interacted with the NBDs of $Gli\alpha_6$ and $Gli\alpha_3$ of another F_1-like ATPase unit, respectively (Fig. 2a, c). These interactions suggest that the Gliβ-specific N-terminal region plays a role in the incorporation of PGK into the twin motor and stabilisation of the ATPase dimer. A difference between Gliα and the F_1-ATPase α subunit is the absence of the H1 helix, which interacts with the peripheral stalk[20] (Extended Data Fig. 9). This absence is consistent with the lack of a gene homologous to the peripheral stalk in the Type 2 ATPase gene cluster[12]. Gliγ, which is composed of a coiled coil and an α/β fold typical of the F_1-ATPase γ subunit,

was superimposed on the γ subunit of the *Bacillus* PS3 F_1-ATPase with an RMSD value of 5.79 Å for Cα atoms due to a lower sequence conservation than that of the catalytic subunits[15] (Fig. 1j, k). The folded C-terminal α-helix, which is 25 Å longer than the F_1-ATPase γ subunit, protrudes from the N-terminal side of the hexameric ring and interacts with the crowns of Gliαβ (Fig. 1k, Extended Data Fig. 10a, b). The coiled coil of Gliγ hydrophobically interacted with the CTDs of Gliαβ in the hexameric ring (Extended Data Fig. 10c), and in the F_1-ATPase, this interaction is involved in axle hold and torque transmission[21].

Accessories of dimeric F_1-like ATPase

Generally, PGK is bifurcated into two domains interconnected by an α-helix: the NTD, which binds to 3-phosphoglycerate (3-PG) or 1,3-bisphosphoglycerate (1,3-BPG), and the CTD, which binds to Mg-ADP or Mg-ATP[22] (Extended Data Fig. 11a). The twin-motor PGK structure, comprising the CTD and a segment of the α-helix, exhibited a high structural similarity to the PGK from *S. aureus* (PDB ID: 4DG5), with an RMSD value of 3.12 Å for Cα atoms (Extended Data Fig. 11b, c). The β loop of the PGK-CTD invades the depression of the folded Gliβ-NTD and interacts with the H2 helix and the H2–H3 loop of the Gliβ-NTD (Fig. 2d). The H4–β loop and H5 helix of the PGK-CTD also interacted with the H5 and H4 helices of the Gliβ-NTD, respectively. Nucleotide-derived densities were not found in the PGK-CTD of the twin motor, despite conservation of the residues important for nucleotide binding in PGK[23] (Extended Data Figs. 11d–f, 12). None of the twin-motor PGK-NTDs were modelled due to the poor densities of the reconstruction. However, the binding and catalytic residues for 3-PG or 1,3-BPG in PGK were conserved in terms of amino acid sequence, suggesting that the

twin-motor PGK possesses enzymatic activity (Extended Data Fig. 12). As the binding and catalytic residues were not conserved in another PGK homologue, MMOB4490, encoded in the *M. mobile* genome, the twin-motor PGK is expected to function as the original PGK in glycolysis (Extended Data Fig. 12). The GliD ($GliD_{1,3,4,6}$) bridge components formed dimers at the interface of two F_1-like ATPase units, whereas $GliD_{2,5}$ at the twin-motor end existed as monomers (Fig. 2a, e, f). GliD contained a globular domain and an N-terminal long α-helix (H2), which was only visualised in the dimer. The globular domain interacted with the H20–H25 region at the C-terminus of Gliα (Fig. 2g, h). The two H2 helices in the GliD dimer aligned parallel to each other across the H20–H25 region of Gliα, GliE, Gliβ-NTD, and Gliβ-CTD (Fig. 2f). These two α-helices are reminiscent of the dynein buttress that connects the AAA+ ring and the tubulin-binding domain[24], suggesting a regulatory role for structural changes induced by the ATPase activity of the F_1-like ATPase units.

Structural information suggesting a catalytic mechanism analogous to that of F_1-ATPase

The crown region of the hexameric ring exhibited approximately six-fold rotational symmetry, whereas the CTD region was asymmetric (Extended Data Fig. 10a). This observation suggests a structural change with a pivot point between the crown and CTD. $Gli\beta_{1–3}$ adopted three distinct conformations, which appear to be the transition states of CTD flexion motion towards Gliγ, with a positional difference of 11 Å for the DELSEED loop (Fig. 3a). These conformations were named $Gli\beta_C$ (closed), $Gli\beta_{HO}$ (half-open), and $Gli\beta_O$ (open), according to the conformation names of F_1-ATPase[8]. The conformations were arranged clockwise when viewed from the C-terminus of the

hexameric ring (Fig. 3b). These conformations resemble the states referred to as *ATP-waiting* or *step-waiting*, which occurs during the catalytic reaction of *Bacillus* PS3 F_1-ATPase; the latter occurs after ATP binding[8] (Extended Data Table 3). In Gliα, the region corresponding to the DELSEED loop exhibited only a 5 Å difference in position relative to the Gliγ side, whereas the H20–H25 region interacting with GliD exhibited a difference of 9 Å (Extended Data Fig. 13). These conformations were named $Gli\alpha_C$ (close), $Gli\alpha_{HO}$ (half-open), and $Gli\alpha_O$ (open) based on the H20–H25 positions viewed from the Gliγ side. If this difference in Gliα represents a conformational change associated with ATP hydrolysis of the twin motor, force transfer may occur from F_1-like ATPase to GliD. The catalytic sites formed at the α–β interface of $Gli\alpha_C\beta_C$ and $Gli\alpha_{HO}\beta_{HO}$ contained Mg-ATP and Mg-ADP + P_i, respectively, whereas no nucleotide density was found at the catalytic site of $Gli\alpha_O\beta_O$ (Fig. 3b–d, Extended Data Fig. 14). The nucleotide-binding states were also shared between the two F_1-like ATPases according to the pseudo-two-fold rotational symmetry. The residues of F_1-ATPase involved in ATP hydrolysis, including those in the arginine finger, were conserved in Gliαβ, suggesting a shared ATP hydrolysis pathway between F_1-ATPase and the twin motor (Fig. 3d). Mg-ATP was observed at the remaining three interfaces, hereafter referred to as the β–α interfaces (Fig. 3b, Extended Data Fig. 14). At the β–α interface, Gliα-K179 corresponded to the position of conserved residue Q200 of the F_1-ATPase α subunit (Extended Data Fig. 15a, b). Compared with the α–β interface, Gliα-K179 is charge inverted relative to the glutamate essential for the catalytic activity (E190 of the F_1-ATPase β subunit), suggesting that the β–α interface, akin to F_1-ATPase, does not exhibit ATP hydrolysis activity (Extended Data Fig. 15c). The conformational sequence pattern of three Gliβ subunits with bound nucleotides was identical to that of the

ATP-waiting state of F_1-ATPase[8] (Fig. 3b). These data suggest that Mg-ATP binding to the catalytic site of Gli$\alpha_O\beta_O$ promotes the catalytic reaction of the entire F_1-like ATPase based on the catalytic mechanism analogous to that of F_1-ATPase.

Twin motors in the chain

The atomic model of the twin motor was fitted into the previously reconstructed density of the internal chain, obtained using negative staining electron microscopy (EM) SPA[2] (Fig. 4a). To circumvent misfitting of the long-axis orientation of the twin motors due to the low-resolution density map (29.7 Å) of the chain structure, regions with asymmetric structures, such as the NTDs of Gli$\beta_{3,6}$, GliE, and PGK_3, were excluded from the fitted model. At the interface between twin-motor units, GliDs that project along the long axis of the twin motor faced each other, suggesting their role as a linker for chain formation. However, the 3D map of the internal chain revealed a remaining density at the interface that cannot be filled by GliDs, which may correspond to the approximately 100 residues comprising an N-terminal region and loops that have not been modelled.

Discussion

The major difference between the twin motor and the dimeric form of eukaryotic mitochondrial ATP synthases[5] is the interaction between the F_1 domains through GliD and the N-terminal region of Gliβ. Although the GliD dimer does not have a transmembrane segment, the two long α-helices at the N-terminus are reminiscent of the structure of a peripheral stalk. This observation is consistent with the hypothesis that the MMOB1620 gene encoding GliD is derived through gene fusion from the b and δ subunits, which comprise the peripheral stalk[15]. The GliD-mediated dimer and chain

formation may allow F_1-like ATPase units to work cooperatively. Consistently, changes in the distance between twin motors have been associated with the ATP hydrolysis reaction, suggesting force transfer between the twin motors through GliD[3,4]. The PGK in the twin motor may efficiently supply ATP to the ATPase as fuel. Further, PGK molecules protruding from the transverse axis of the twin motor may be involved in the sheet formation of the internal chain, according to negative staining EM[25]. The weak density of PGK in the cryo-EM map can be explained by its flexibility, which was identified using high-speed atomic force microscopy[2]. The flexibility of the PGK molecule may suggest that the chain sheet serves as a cytoskeleton to withstand mechanical stress in the mycoplasma cell, which does not have a cell wall. The GliE subunit, which is bound to only one side of the dimeric F_1-like ATPase, creates asymmetry in the twin motor structure and may contribute to the unidirectional nature of the gliding motility. However, this protein may also bind to another side of the dimeric F_1-like ATPase in the cell but dislodge during purification.

The three distinct forms of the catalytic subunit Gliβ and their corresponding nucleotide binding suggest a rotary catalytic mechanism analogous to that of the rotary ATPases (Fig. 4b). In this rotary catalytic mechanism, $Gli\alpha_O\beta_O$ transitions to $Gli\alpha_C\beta_C$, and the DELSEED loop of Gliβ in this transition approaches Gliγ upon ATP binding at the catalytic site. The other Gliαβ dimers in the hexameric ring also operate cooperatively, with $Gli\alpha_C\beta_C$ transitioning to $Gli\alpha_{HO}\beta_{HO}$ upon ATP hydrolysis and $Gli\alpha_{HO}\beta_{HO}$ transitioning to $Gli\alpha_O\beta_O$ upon ADP and phosphate release. This one-step conformational change of the hexameric ring prompts a 120° rotation of Gliγ. Each Gliαβ dimer sequentially hydrolyses ATP, and through a three-step process, the hexameric ring structure and position of Gliγ revert to their initial states. The pseudo-two-fold

rotational symmetry structure of the twin motor suggests that the two F_1-like ATPase units operate in a synchronised manner, maintaining the structural symmetry. Throughout the catalytic reaction, significant changes in the positioning of the two F_1-like ATPase units within the twin motor may be hindered due to the presence of the N-terminal regions of Gliβ bridging the two units and a buttress-like structure composed of two long α-helices of the GliD dimer (Fig. 2a, c, f).

For cell gliding, the rotary motions of the twin motors must be converted into a linear motion. This conversion mechanism may occur due to the membrane protein Gli521, which consists of a hook and rod, thereby functioning as a crank[26] (Fig. 4c). Upon the conversion of the rotary motion to linear motion, Gli521 pulls the leg protein, Gli349, which is bound to sialylated oligosaccharides on the host cell surface, thereby propelling the mycoplasma cell forward[27]. The presence of a globular domain in Gliγ, similar to that in the F_1-ATPase γ subunit, suggests a potential interaction with a membrane-embedded F_o-like domain. MMOB1610 and MMOB1650, encoded in the Type 2 ATPase gene cluster, possess 12 and 2 transmembrane segments, respectively[15]. These two proteins are potential interaction partners for the globular domain of Gliγ at the cell membrane, transmitting the rotary motion to Gli521 on the cell surface.

The roles of rotary ATPases and their relatives, such as the flagellar type III protein export apparatus, which exhibit a hexameric ring with a central shaft, involve protein and ion transport[28,29]. We hypothesised that F_1F_o-ATPase has acquired the role and mechanism of the twin motor through an incidental contact with an adhesin on the membrane during the evolution of mycoplasma from a non-motile to a motile state[2,30]. This primitive gliding motility would have conferred a survival advantage. Another F_1-like ATPase, referred to as Type 3 ATPase, is also found in mycoplasma, and this

F_1-like ATPase may drive the system that cleaves host antibodies[12,31]. Notably, Type 2 and 3 ATPases transition from F_1-ATPase to drive mycoplasma-specific systems. Understanding these unique F_1-like ATPases will contribute to investigations into the working principles and evolution of rotary ATPases.

References

1. Stewart, A. G., Sobti, M., Harvey, R. P. & Stock, D. Rotary ATPases. *Bioarchitecture* **3**, 2–12 (2013).
2. Toyonaga, T. *et al.* Chained structure of dimeric F1-like ATPase in *Mycoplasma mobile* gliding machinery. *mBio* **12**, e0141421 (2021).
3. Nishikawa, M. S. *et al.* Refined mechanism of *Mycoplasma mobile* gliding based on structure, ATPase activity, and sialic acid binding of machinery. *mBio* **10**, e02846-19 (2019).
4. Kobayashi, K. *et al.* Movements of *Mycoplasma mobile* gliding machinery detected by high-speed atomic force microscopy. *mBio* **12**, e0004021 (2021).
5. Kühlbrandt, W. Structure and mechanisms of F-Type ATP synthases. *Annu Rev Biochem* **88**, 515–549 (2019).
6. Nakane, D. & Miyata, M. Cytoskeletal ‘jellyfish’ structure of *Mycoplasma mobile*. *Proc Natl Acad Sci U S A* **104**, 19518–19523 (2007).
7. Noji, H. & Ueno, H. How Does F1-ATPase Generate Torque?: Analysis From Cryo-Electron Microscopy and Rotational Catalysis of Thermophilic F1. *Front Microbiol* **13**, 904084 (2022).
8. Nakano, A., Kishikawa, J. ichi, Mitsuoka, K. & Yokoyama, K. Mechanism of ATP hydrolysis dependent rotation of bacterial ATP synthase. *Nat Commun* **14**,

4090 (2023).

9. Noji, H., Yasuda, R., Yoshida, M. & Kinosita, K. Direct observation of the rotation of F1-ATPase. *Nature* **386**, 299–302 (1997).

10. Abrahams, J. P., Leslie, A. G. W., Lutter, R. & Walker, J. E. Structure at 2.8 Å resolution of F1-ATPase from bovine heart mitochondria. *Nature* **370**, 621–628 (1994).

11. Tulum, I., Kimura, K. & Miyata, M. Identification and sequence analyses of the gliding machinery proteins from *Mycoplasma mobile*. *Scientific Reports 2020 10:1* **10**, 1–11 (2020).

12. Béven, L. *et al*. Specific evolution of F1-like ATPases in mycoplasmas. *PLoS One* **7**, e38793 (2012).

13. Bredt, W. & Radestock, U. Gliding motility of *Mycoplasma pulmonis*. *J Bacteriol* **130**, 937 (1977).

14. Rosengarten, R. & Kirchhoff, H. Gliding motility of Mycoplasma sp. nov. strain 163K. *J Bacteriol* **169**, 1891–1898 (1987).

15. Miyata, M. & Hamaguchi, T. Prospects for the gliding mechanism of *Mycoplasma mobile*. *Curr Opin Microbiol* **29**, 15–21 (2016).

16. Fujita, J. *et al*. Epoxidized graphene grid for highly efficient high-resolution cryoEM structural analysis. *Sci Rep* **13**, 2279 (2023).

17. Leimgruber, R. M. & Senior, A. E. Removal of ‘tightly bound’ nucleotides from phosphorylating submitochondrial particles. *Journal of Biological Chemistry* **251**, 7110–7113 (1976).

18. Menz, R. I., Walker, J. E. & Leslie, A. G. W. Structure of bovine mitochondrial F(1)-ATPase with nucleotide bound to all three catalytic sites: implications for

the mechanism of rotary catalysis. *Cell* **106**, 331–341 (2001).

19. Tanigawara, M. *et al.* Role of the DELSEED Loop in Torque Transmission of F1-ATPase. *Biophys J* **103**, 970–978 (2012).

20. Sobti, M. *et al.* Cryo-EM structures of the autoinhibited *E. coli* ATP synthase in three rotational states. *Elife* **5**, e21598 (2016).

21. Kohori, A. *et al.* Torque generation in F1-ATPase devoid of the entire amino-terminal helix of the rotor that fills half of the stator orifice. *Biophys J* **101**, 188–195 (2011).

22. Bowler, M. W. Conformational dynamics in phosphoglycerate kinase, an open and shut case? *FEBS Lett* **587**, 1878–1883 (2013).

23. Rojas-Pirela, M. *et al.* Phosphoglycerate kinase: structural aspects and functions, with special emphasis on the enzyme from Kinetoplastea. *Open Biol* **10**, 200302 (2020).

24. Rao, L., Berger, F., Nicholas, M. P. & Gennerich, A. Molecular mechanism of cytoplasmic dynein tension sensing. *Nature Communications 2019 10:1* **10**, 1–17 (2019).

25. Fukushima, M., Toyonaga, T., Tahara, Y. O., Nakane, D. & Miyata, M. Internal structure of *Mycoplasma mobile* gliding machinery analyzed by negative staining electron tomography. *Biophys Physicobiol* e210015 (2024).

26. Nonaka, T., Adan-Kubo, J. & Miyata, M. Triskelion structure of the Gli521 protein, involved in the gliding mechanism of *Mycoplasma mobile*. *J Bacteriol* **192**, 636–642 (2010).

27. Hamaguchi, T., Kawakami, M., Furukawa, H. & Miyata, M. Identification of novel protein domain for sialyloligosaccharide binding essential to *Mycoplasma*

mobile gliding. *FEMS Microbiol Lett* **366**, fnz016 (2019).

28. Ibuki, T. *et al.* Common architecture of the flagellar type III protein export apparatus and F- and V-type ATPases. *Nat Struct Mol Biol* **18**, 277–282 (2011).

29. Majewski, D. D. *et al.* Cryo-EM structure of the homohexameric T3SS ATPase-central stalk complex reveals rotary ATPase-like asymmetry. *Nat Commun* **10**, 626 (2019).

30. Miyata, M. *et al.* Tree of motility - A proposed history of motility systems in the tree of life. *Genes. Cell* **25**, 6–21 (2020).

31. Nottelet, P. *et al.* The mycoplasma surface proteins MIB and MIP promote the dissociation of the antibody-antigen interaction. *Sci Adv* **7**, eabf2403 (2021).

32. Aluotto, B. B., Wittler, R., Williams, C. & Faber, J. Standardized bacteriologic techniques for the characterization of Mycoplasma species1, 2. *Int J Syst Evol Microbiol* **20**, 35–58 (1970).

33. Miyata, M. *et al.* Gliding mutants of *Mycoplasma mobile*: relationships between motility and cell morphology, cell adhesion and microcolony formation. *Microbiology (Reading)* **146 (Pt 6)**, 1311–1320 (2000).

34. Uenoyama, A., Seto, S., Nakane, D. & Miyata, M. Regions on Gli349 and Gli521 protein molecules directly involved in movements of *Mycoplasma mobile* gliding machinery, suggested by use of inhibitory antibodies and mutants. *J Bacteriol* **191**, 1982–1985 (2009).

35. Mizutani, M., Tulum, I., Kinosita, Y., Nishizaka, T. & Miyata, M. Detailed analyses of stall force generation in *Mycoplasma mobile* gliding. *Biophys J* **114**, 1411–1419 (2018).

36. Hellman, U., Wernstedt, C., Góñez, J. & Heldin, C. H. Improvement of an

'In-Gel' digestion procedure for the micropreparation of internal protein fragments for amino acid sequencing. *Anal Biochem* **224**, 451–455 (1995).

37. Fujita, J. *et al.* Structures of a FtsZ single protofilament and a double-helical tube in complex with a monobody. *Nat Commun* **14**, 4073 (2023).

38. Mastronarde, D. N. Automated electron microscope tomography using robust prediction of specimen movements. *J Struct Biol* **152**, 36–51 (2005).

39. Punjani, A., Rubinstein, J. L., Fleet, D. J. & Brubaker, M. A. cryoSPARC: algorithms for rapid unsupervised cryo-EM structure determination. *Nat Methods* **14**, 290–296 (2017).

40. Zivanov, J. *et al.* A Bayesian approach to single-particle electron cryo-tomography in RELION-4.0. *Elife* **11**, e83724 (2022).

41. Bepler, T., Kelley, K., Noble, A. J. & Berger, B. Topaz-Denoise: general deep denoising models for cryoEM and cryoET. *Nat Commun* **11**, 5208 (2020).

42. Jumper, J. *et al.* Highly accurate protein structure prediction with AlphaFold. *Nature* **596**, 583–589 (2021).

43. Šali, A. & Blundell, T. L. Comparative protein modelling by satisfaction of spatial restraints. *J Mol Biol* **234**, 779–815 (1993).

44. Pettersen, E. F. *et al.* UCSF Chimera--a visualization system for exploratory research and analysis. *J Comput Chem* **25**, 1605–1612 (2004).

45. Emsley, P., Lohkamp, B., Scott, W. G. & Cowtan, K. Features and development of Coot. *Acta Crystallogr D Biol Crystallogr* **66**, 486–501 (2010).

46. Afonine, P. V. *et al.* Real-space refinement in PHENIX for cryo-EM and crystallography. *Acta Crystallogr D Struct Biol* **74**, 531–544 (2018).

47. Liebschner, D. *et al.* Macromolecular structure determination using X-rays,

neutrons and electrons: recent developments in Phenix. *Acta Crystallogr D Struct Biol* **75**, 861–877 (2019).

48. Pintilie, G. *et al*. Measurement of atom resolvability in cryo-EM maps with Q-scores. *Nat Methods* **17**, 328–334 (2020).

49. Yamashita, K., Palmer, C. M., Burnley, T. & Murshudov, G. N. Cryo-EM single-particle structure refinement and map calculation using Servalcat. *Acta Crystallogr D Struct Biol* **77**, 1282–1291 (2021).

50. Pettersen, E. F. *et al*. UCSF ChimeraX: Structure visualization for researchers, educators, and developers. *Protein Science* **30**, 70–82 (2021).

Figure legends

Fig. 1 Structure of the twin motor featuring dimeric F_1-like ATPase.

(**a**) Gliding machinery of *Mycoplasma mobile*. Overall view of the gliding machinery (top) and part of the internal chain (bottom). (**b**) Overall structure of the twin motor. The illustration is drawn in the upper left. Scale bar = 25 Å. (**c**) Atomic model of the twin motor. Black triangles represent nucleotides. Maps in (b) and (c) are contoured at 0.55 in UCSF ChimeraX. (**d**) Dimeric F_1-like ATPase in the twin motor. Dotted lines indicate the axis of each ATPase. (**e**) Density of Mg-ATP bound to F_1-like ATPase. The dotted region in (c) is shown. (**f, h, j**) Subunits constituting F_1-like ATPase. (**g, i, k**) Overlay of subunits of F_1-like ATPase and *Bacillus* PS3 F_1-ATPase. The subunits of the *Bacillus* PS3 F_1-ATPase, αβ (PDB ID: 8HH5) and γ (PDB ID: 8HH2), are coloured purple.

Fig. 2 Interaction between subunits.

(**a**) N- and C-terminal regions of the twin motor. The twin motor is viewed from the top

of the illustration. Arrows indicate the interface between dimeric F_1-like ATPases. Maps are contoured at 0.55 in UCSF ChimeraX. (**b**) Structure of Gliβ and PGK. (**c**) Interaction between the N-terminal region of Gliβ and Gliα-NBD at the interface between dimeric F_1-like ATPases. The dotted region in (a) is shown. (**d**) Interaction of PGK with the Gliβ-NTD. The dotted region in (a) is shown. (**e**) Structure of the Gliα and GliD monomers. (**f**) GliD dimer at the interface between dimeric F_1-like ATPases. The figure corresponds to the dotted region in the illustration. (**g, h**) Interaction between GliD and Gliα-CTD. Each corresponds to the dotted regions in (f).

Fig. 3 Structural conformations and nucleotide binding of Gliβ.

(**a**) Differences in the conformations of the three Gliβ. Superposed three Gliβs in the F_1-like ATPase. The dotted lines indicate the position of the DELSEED loop of each Gliβ. (**b**) Nucleotide binding pattern of dimeric F_1-like ATPase and F_1-ATPase. The catalytic site is circled by black dotted lines. (**c**) Gliαβ dimer in each conformation in the hexamer. (**d**) Comparison of the catalytic sites. Each catalytic site corresponds to the dot square above. The catalytic sites are superimposed on the corresponding catalytic sites of F_1-ATPase (PDB ID: 8HHA), which are coloured purple.

Fig. 4 Structure and motion of the gliding machinery.

(**a**) Fitting of the atomic model of the twin-motor into the EM map of the motor chain. The right panel indicates the interface between GliDs. (**b**) Possible rotational catalytic mechanism of F_1-like ATPase. Gliγ is indicated by yellow arrows, the direction of which indicates the conformational tilt. (**c**) A possible explanation for the conversion mechanism from rotational to linear motion. Dotted arrows indicate unknown force

transduction in the cell membrane. Gli349 and Gli521 are depicted in red and green, respectively. Unidentified protein regions in the gliding machinery are coloured purple.

Methods

Optical microscopy

The cells of the *M. mobile* mutant strain (gli521 [P476R]), which can glide like the wild type strain but binds sialylated oligosaccharides more tightly, were cultured, observed using phase-contrast microscopy, and recorded as previously described[32–35]. The recorded video was analysed using ImageJ software v1.54d (https://imagej.nih.gov/ij/).

Isolation of the twin motor

The twin motor was isolated from the *M. mobile* mutant strain (gli521 [P476R]), as previously described[2]. The twin motor sample with phosphate-buffered saline (PBS) consisting of 8.1 mM Na_2HPO_4, 1.5 mM KH_2PO_4 (pH 7.3), 2.7 mM KCl and 137 mM NaCl, and 1 mM $MgCl_2$ was concentrated to 1 mg/mL using a 100K Vivaspin concentrator (Merck, Germany) with 0.1% (w/v) CHAPS to prevent membrane adsorption. The concentrated twin-motor was subjected to 12.5% SDS-PAGE and stained using Coomassie brilliant blue R-250. The bands of the component proteins were identified using peptide mass fingerprinting, as previously described[36].

Cryo-EM grid preparation and data acquisition

An EG-grid was prepared as previously described[37]. A 2.6 μL sample solution was applied on the grid, automatically blotted from both sides with filter paper at 4 °C for 2 s at 100% humidity, and vitrificated using the semi-automated vitrification device,

Vitrobot Mark IV (Thermo Fisher Scientific, USA). Cryo-EM imaging was performed using a CRYO ARM 300 (JEOL, Japan) operated at 300 kV with a K3 direct electron detector camera (AMETEK, Gatan, USA). A total of 7,350 movies were recorded using SerialEM software[38] with a total dose of approximately 80 electrons $Å^{-2}$ for 40 frames, an exposure time of 3.3 s per movie, and a nominal defocus range of −0.8 to −1.8 µm. The nominal magnification was 60,000×, corresponding to 0.87 Å per pixel.

Cryo-EM image processing

The image processing steps for SPA are summarised in Extended Data Figs. 3 and 4. Image processing was performed using cryoSPARC v3.3.2[39], unless otherwise stated. Movies were aligned using patch-based motion correction, and the contrast transfer function (CTF) parameters were estimated using patch CTF estimation. Micrographs with a CTF fit resolution worse than 8 Å were removed. Particles were automatically picked up using a Blob Picker, extracted with ×4 binning, and 2D-classified. The obtained 2D averaged images were used as templates for the Template Picker to pick up good particles. After two rounds of 2D classification, the selected good particles were subjected to local motion correction and re-extracted with the original pixel size. The particles were subjected to Ab-initio reconstruction using C1 symmetry enforced with a final resolution limit of 12−Å and heterogeneous reconstruction with 3 classes. Particles in class 2 were subjected to homogeneous reconstruction using C1 symmetry, resulting in a map at a resolution of 3.5−Å. The final map was generated via local and global CTF refinement, and then non-uniform refinement. To improve the local resolution, the final map and particles were subjected to particle subtraction and local refinement using C1 symmetry to generate half-divided maps, each containing a

monomeric ATPase. The whole and two local maps were subjected to mask creation and postprocessing in RELION 4.0[40], resulting in resolutions of 3.2, 3.1, and 3.1 Å, respectively. Local resolution estimation was also performed in RELION 4.0. The post-processed map was denoised using Topaz software v0.2.5 with the trained model Unet-3d-10a[41]. RELION 4.0 was used to calculate the Fourier shell correlation (FSC) curve between two half-maps and estimate the local resolution.

Modelling

Initial models for GliαβγDE were generated using AlphaFold2[42], whereas the homology model for PGK was generated using Modeller v10.4[43] with the atomic model of PGK (PDB ID: 4DG5) from *S. aureus*. The generated models were fitted to the corresponding densities of the EM map as rigid bodies using UCSF Chimera v1.15[44]. The fitted models were manually inspected and adjusted using COOT v0.9.8.1[45] and refined using the *phenix.real_space_refine* program in PHENIX v1.19[46,47] with reference model restraints using atomic models of F_1-ATPase (PDB ID: 5IK2) from *Caldalaklibacillus thermarum* and PGK (PDB ID: 3ZLB) from *Streptococcus pneumoniae*. Manual adjustment using COOT and refinement using PHENIX were repeated until model parameters were no longer improved. FSC curves between the map and model were calculated using PHENIX. The refined model was also evaluated via comprehensive validation in PHENIX and the Q-score[48]. To identify the nucleotide binding sites of F_1-like ATPases, F_o-F_c maps were generated using Servalcat[49]. Superposition of models and fitting of models to the map were performed using UCSF ChimeraX v1.2.5[50]. All structural figures were obtained using UCSF ChimeraX.

Data availability

The cryo-EM map for the twin motor is available on the Electron Microscopy Data Bank (EMDB) under accession code: EMD-60718. The coordinates have been deposited in the Protein Data Bank (PDB) under accession code: 9IO5.

Acknowledgments

We thank Tomomi Shimonaka at Osaka Metropolitan University and Fumiaki Makino at Osaka University for their technical assistance. This manuscript was edited using Copilot, an AI tool. This study was supported by Grants-in-Aid for Scientific Research (A) (JP17H01544), a JST CREST grant (JPMJCR19S5) to M.M., and Research Support Project for Life Science and Drug Discovery (BINDS) from AMED under Grant Number, JP22am121003, to K.N., and JEOL YOKOGUSHI Research Alliance Laboratories of Osaka University to K.N.

Author contributions

T.T. and M.M. conceived the strategy. M.M. and K.N. supervised the research. T.T. prepared the cryo-EM samples and carried out the biochemical analyses. J.F. prepared EG-grid for cryo-EM observation. A.K. and T.M. performed cryo-EM. T.T. carried out 3D reconstruction and model building. T.K., T.H., A.K., T.M., K.K., and K.N. participated in the discussion regarding the structural analyses. T.T. and M.M. wrote the manuscript with input from all authors.

Competing interests

The authors have declared no competing interest.

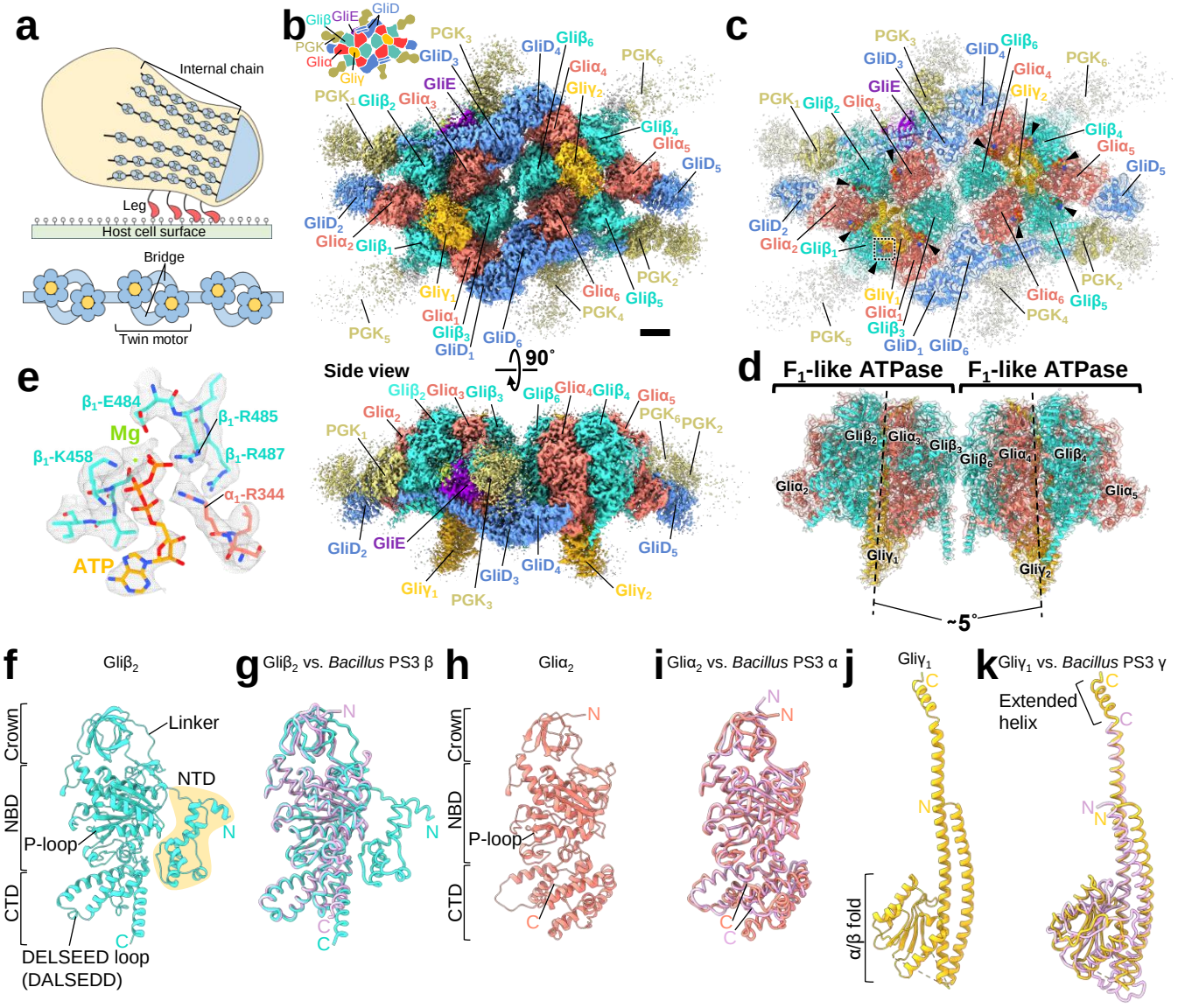
a
Internal chain
Leg
Host cell surface
Bridge
Twin motor
b
c
Side view
90°
d
F1-like ATPase
F1-like ATPase
~5°
e
β1-E484
β1-R485
Mg
β1-K458
β1-R487
α1-R344
ATP
f
Gliβ2
Linker
NTD
Crown
NBD
CTD
P-loop
DELSEED loop
(DALSEDD)
g
Gliβ2 vs. Bacillus PS3 β
h
Gliα2
i
Gliα2 vs. Bacillus PS3 α
j
Gliγ1
α/β fold
k
Gliγ1 vs. Bacillus PS3 γ
Extended
helix

Fig. 1

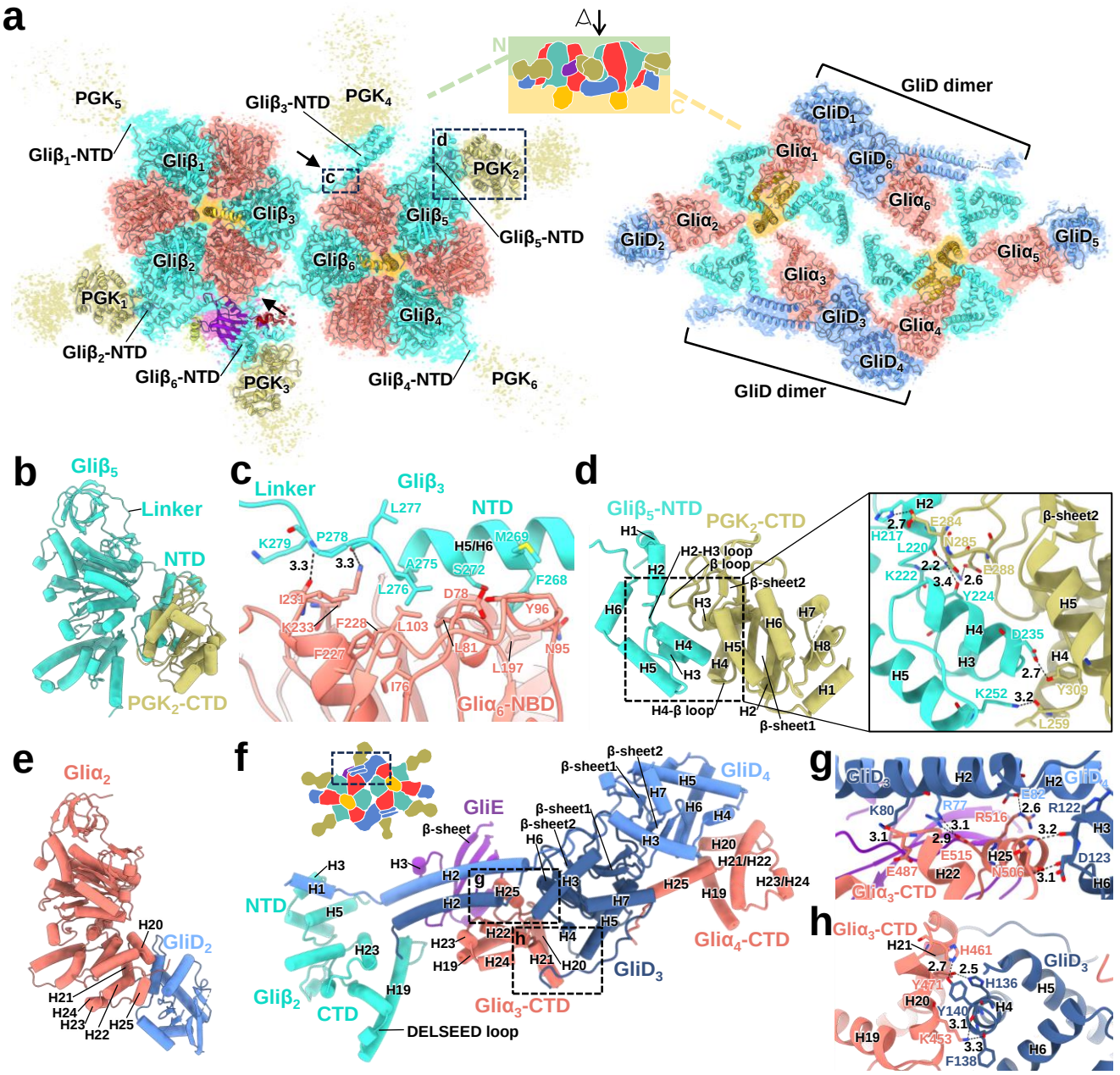
a
A
N
C
PGK5
Gliβ1-NTD
Gliβ1
Gliβ3-NTD
PGK4
c
d
PGK2
Gliβ3
Gliβ5
Gliβ5-NTD
Gliβ2
Gliβ6
PGK1
Gliβ2-NTD
Gliβ6-NTD
PGK3
Gliβ4
Gliβ4-NTD
PGK6
GliD dimer
GliD1
Gliα1
GliD6
Gliα6
Gliα2
GliD2
Gliα5
GliD5
Gliα3
GliD3
Gliα4
GliD4
GliD dimer
b
Gliβ5
Linker
NTD
PGK2-CTD
c
Linker
Gliβ3
NTD
L277
K279
P278
3.3
3.3
H5/H6
M269
A275
S272
F268
L276
D78
I233
Y96
K233
F228
L103
N95
F227
L81
L197
I76
Gliα6-NBD
d
Gliβ5-NTD
PGK2-CTD
H1
H2-H3 loop
β loop
H2
β-sheet2
H3
H6
H7
H6
H4
H5
H8
H5
H3
H4
H1
H4-β loop
H2
β-sheet1
H2
2.7
E284
β-sheet2
H217
L220
N285
2.2
E288
K222
3.4
2.6
Y224
H5
H4
D235
H3
H4
2.7
H5
K252
3.2
Y309
L259
e
Gliα2
H20
GliD2
H21
H24
H23
H22
H25
f
β-sheet2
β-sheet1
GliD4
H5
H7
H6
H4
GliE
β-sheet1
β-sheet2
β-sheet
H6
H3
H20
H21/H22
H3
H3
H2
g
H25
H3
H25
H23/H24
H19
NTD
H1
H2
H7
H5
H5
H22
h
H4
H23
H23
H24
H21
H20
H19
GliD3
Gliα4-CTD
Gliβ2
CTD
H19
Gliα3-CTD
DELSEED loop
g
GliD3
H2
H2
GliD4
E82
K80
R77
R516
2.6
R122
3.1
3.1
3.2
H3
2.9
E515
H25
D123
E487
H22
N506
3.1
H6
Gliα3-CTD
h
Gliα3-CTD
H21
H461
2.7
2.5
GliD3
Y471
H136
H5
H20
Y140
H4
3.1
H19
K453
3.3
H6
F138

Fig. 2

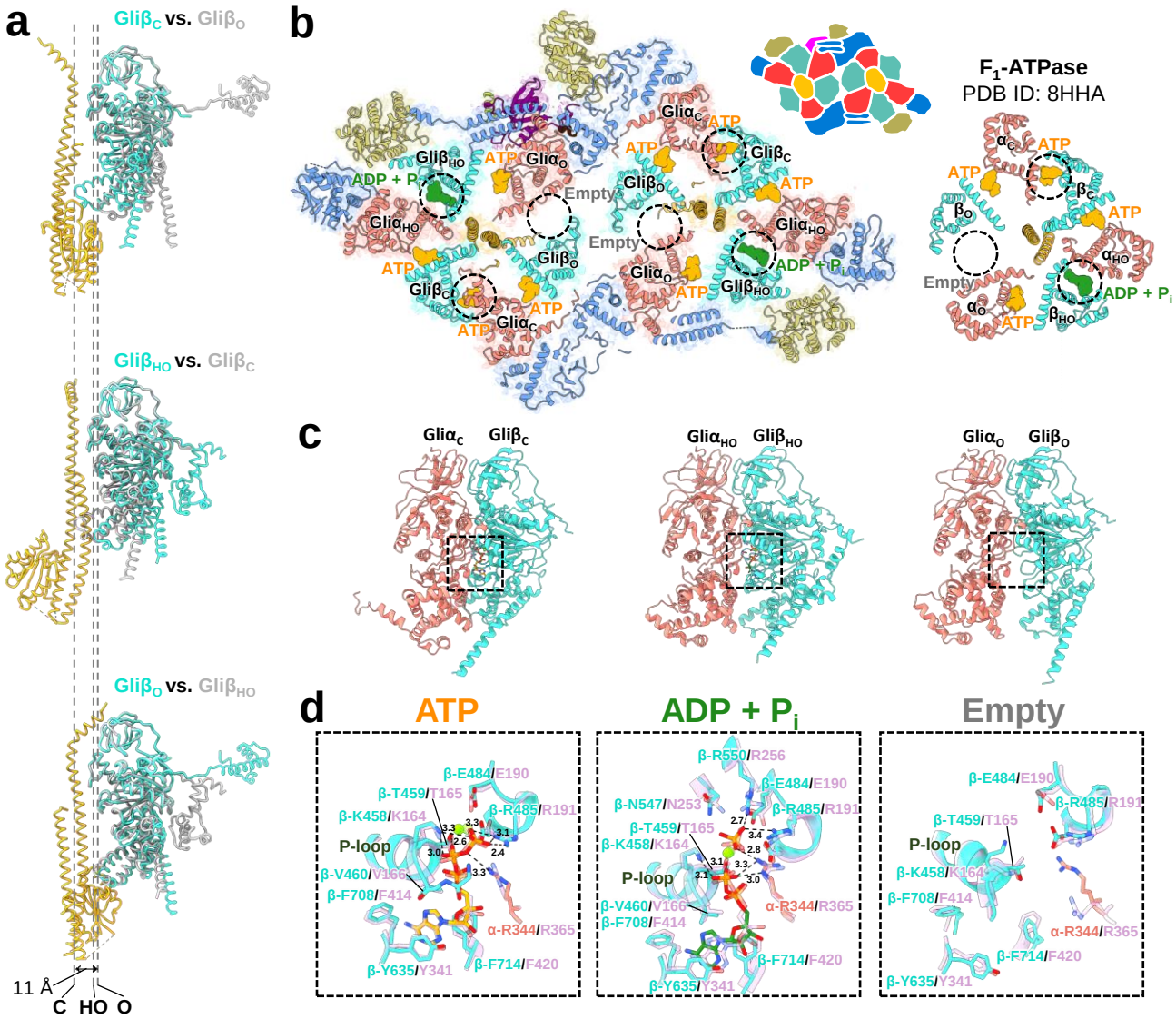
a
Gliβ$_C$ vs. Gliβ$_O$
Gliβ$_{HO}$ vs. Gliβ$_C$
Gliβ$_O$ vs. Gliβ$_{HO}$
11 Å
C HO O
b
F$_1$-ATPase
PDB ID: 8HHA
ADP + P$_i$
ATP
Empty
c
Gliα$_C$ Gliβ$_C$
Gliα$_{HO}$ Gliβ$_{HO}$
Gliα$_O$ Gliβ$_O$
d
ATP
ADP + P$_i$
Empty
P-loop
β-E484/E190
β-T459/T165
β-K458/K164
β-R485/R191
β-V460/V166
β-F708/F414
α-R344/R365
β-F714/F420
β-Y635/Y341
β-R550/R256
β-N547/N253

Fig. 3

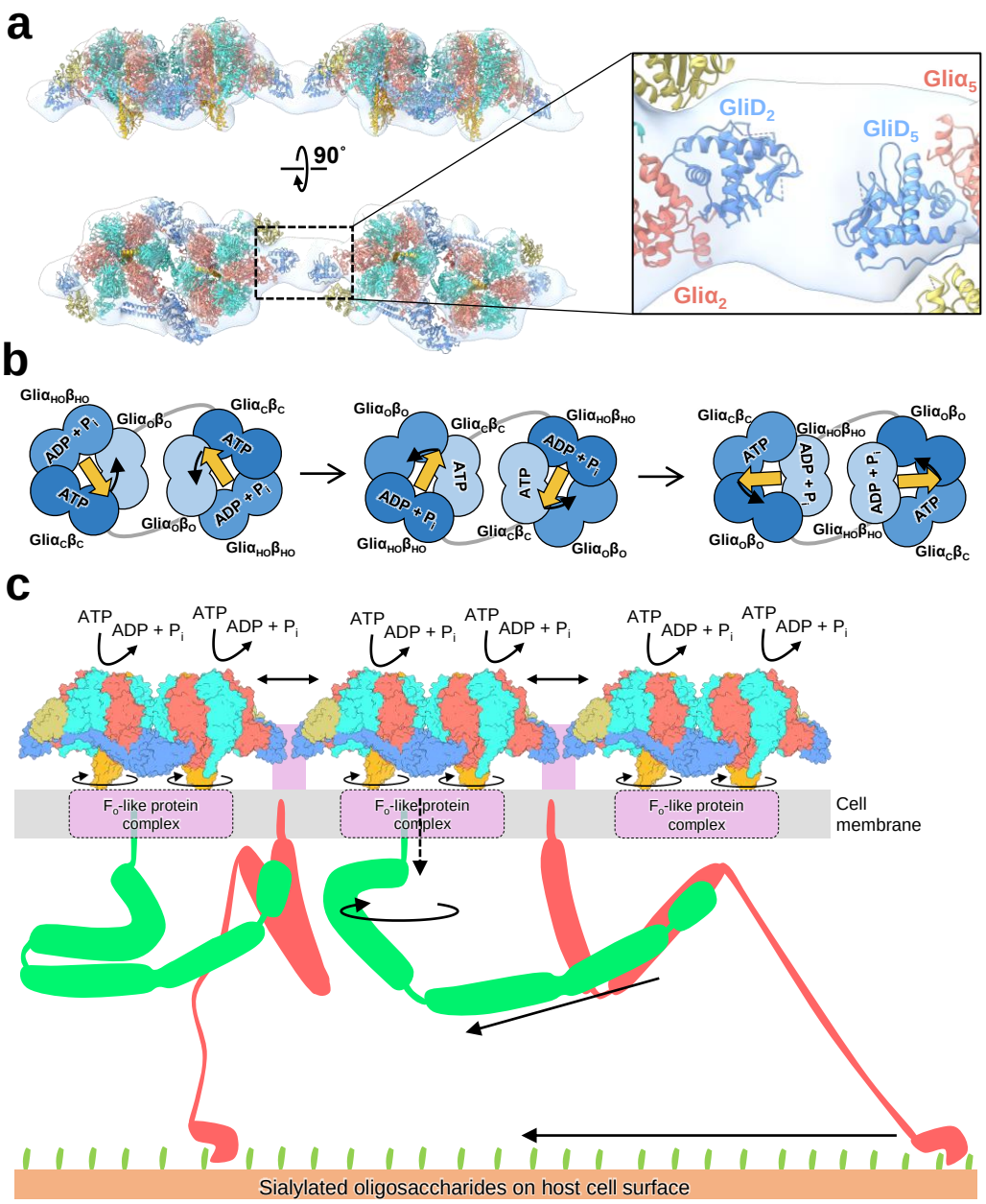
a
90˚
Gliα5
GliD2
GliD5
Gliα2
b
GliαHOβHO
GliαOβO
GliαCβC
ADP + Pi
ATP
c
ATP
ADP + Pi
Fo-like protein complex
Cell membrane
Sialylated oligosaccharides on host cell surface

Fig. 4